Energy Technology
Generation, Conversion, Storage, Distribution
www.entechnol.de

Electrical and Structural Characterization of Large-Format Lithium Iron Phosphate Cells Used in Home-Storage Systems

Mehmet C. Yagci, René Behmann, Viktor Daubert, Jonas A. Braun, Dirk Velten, and Wolfgang G. Bessler*

This article presents a comparative experimental study of the electrical, structural, and chemical properties of large-format, 180 Ah prismatic lithium iron phosphate (LFP)/graphite lithium-ion battery cells from two different manufacturers. These cells are particularly used in the field of stationary energy storage such as home-storage systems. The investigations include 1) cell-to-cell performance assessment, for which a total of 28 cells are tested from each manufacturer; 2) electrical charge/discharge characteristics at different currents and ambient temperatures; 3) internal cell geometries, components, and weight analysis after cell opening; 4) microstructural analysis of the electrodes via light microscopy and scanning electron microscopy; 5) chemical analysis of the electrode materials using energy-dispersive X-ray spectroscopy; and 6) mathematical analysis of the electrode balances. The combined results give a detailed and comparative insight into the cell characteristics, providing the essential information needed for system integration. The study also provides complete and self-consistent parameter sets for the use in cell models needed for performance prediction or state diagnosis.

1. Introduction

Photovoltaic (PV) battery systems for residential power supply, also referred to as home-storage systems, have shown a significant growth over the past years, connected with a strong decrease in prices.[1,2] These batteries have typical energy capacities of 5–15 kWh. Adding a battery to a PV system allows to increase self-sufficiency of the household and self-consumption of the solar energy, therefore contributes to energy independence and reduces the emission of greenhouse gases.[3] Industry-scale storage systems, with energy capacities beyond 15 kWh up to the MWh scale, are also showing increasing growth rates, with additional applicability for peak shaving or grid services.[4]

Both residential-scale and industry-scale storage systems are today mostly based on lithium-ion battery technology.[1] The systems are typically constructed in a modular way, consisting of battery modules which, in turn, include multiple battery cells connected in series and/or in parallel.[5] Knowing and understanding the performance characteristics of the single cells in terms of electrical, thermal, and aging properties is of utmost importance for the design and operation of reliable and long-living systems. These characteristics are often not well known to the system manufacturer, as the cells are typically provided by external suppliers, with only limited information available from data sheets. Therefore, the current study allows to fill the gap between the limited information provided by the cell supplier and the detailed information needed by the system manufacturer.

This study presents a detailed characterization of commercial lithium-ion battery cells from two different manufacturers for the use in home-storage systems. Both cell types are large-format prismatic cells with nominal capacities of 180 Ah. The cell chemistries, as confirmed in the present study, are lithium iron phosphate ($LiFePO_4$, LFP) at the positive electrode and graphite at the negative electrode. The published literature on such large-format cells is scarce. The terms "large cell" or "large-format cell" are used inconsistently in the literature, recent studies including comparatively small cell capacities of 9,[6] 10,[7] 20,[8] 25,[9] or around 50 Ah.[10–12] There is very little literature available on cells with capacities beyond 100 Ah. Li et al.[13] presented the fabrication and testing of 100 Ah LFP/graphite pouch cells. Bacci et al.[14] performed cycling tests with 100 Ah LFP cells and compared the results with existing capacity fade models. Panchal et al.[15] measured the aging characteristics of 200 Ah LFP/graphite cells used for an electric vehicle. To the best of our knowledge, the detailed analysis conducted in this article has not been published before on such large cells.

Modeling and simulation play an increasingly important role in lithium-ion battery development.[16] Physicochemical models

M. C. Yagci, R. Behmann, V. Daubert, J. A. Braun, Prof. D. Velten, Prof. W. G. Bessler
Institute of Energy Systems Technology (INES)
Offenburg University of Applied Sciences
Badstrasse 24, Offenburg 77652, Germany
E-mail: mehmet.yagci@hs-offenburg.de

The ORCID identification number(s) for the author(s) of this article can be found under https://doi.org/10.1002/ente.202000911.

DOI: 10.1002/ente.202000911

(often referred to as "Newman" models[17]) are used to support cell design.[18,19] Equivalent circuit models are used in battery management systems.[20] The determination of the required model parameters often requires a major effort. This is true, in particular, for microstructural parameters of the electrode needed for physicochemical models, including the volume fractions and stoichiometry ranges (also referred to as "balancing") of the active materials. Moreover, as model parameters are often compiled from different sources, the self-consistency of the chemical and structural parameters requires special attention.[21] The current study provides not only the empirical data base, but also the necessary mathematical analysis to derive complete and self-consistent sets of cell parameters needed for modeling.

The present investigations include 1) assessment of the cell-to-cell performance scatter, for which a total of 28 cells were tested from each manufacturer; 2) electrical charge/discharge characteristics at different currents and ambient temperatures; 3) internal cell geometries, components, and weight analysis after cell opening; 4) microstructural analysis of the electrodes via light microscopy and scanning electron microscopy (SEM); 5) chemical analysis of the electrode materials using energy-dispersive X-ray spectroscopy (EDX); and 6) use of the data for mathematical analysis of the electrode balances, i.e., lithium stoichiometry ranges during cycling. The combined results provide a detailed and comparative insight into the electrical, electrochemical, thermal, and structural cell characteristics of the two investigated cell types. The investigation of the aging characteristics of the cells will be presented separately.[22] In Section 2, we will describe the cells and the experimental methodology. Section 3 will present and discuss the results along the methodology described above Section 4 will summarize and conclude the study.

2. Experimental Section

2.1. Investigated Cells

We have investigated lithium-ion battery cells from two different Chinese manufacturers, Shenzen Sinopoly Battery Co. Ltd. ("Sinopoly") and China Aviation Lithium Battery Co. Ltd. ("Calb"), with main application in the field of stationary storage. For brevity, in the remainder of this article, the two cell types will be labeled with "Sinopoly" and "Calb." Both cell types have a prismatic geometry, as shown in **Figure 1**. The characteristics according to the data sheets are shown in **Table 1**. Both cell types have a nominal capacity of 180 Ah and a nominal voltage of 3.2 V. The chemistry is not specified in the data sheets, although Sinopoly claims to use "$LiFeYPO_4$" as material, that is, an yttrium-doped lithium iron phosphate.[23] It can be noted that the cutoff voltages are quite different for the two cell types despite the same nominal voltage. For the current study, a total of 28 single cells were investigated from each manufacturer.

2.2. Electrical Characterization

The electrical characterization consisted of charge/discharge cycling at different C-rates (Biologic VMP3, Basytec XCTS, Basytec GSM) and at different ambient temperatures (climate chambers CTS 40/200 Li and Binder KB 115). Cell surface temperature was measured at the center of the cell face

Figure 1. Photographs of the studied cells: Sinopoly (left) and Calb (right).

Table 1. Characteristic data of the two studied cells according to the manufacturers' data sheets.

	Sinopoly	Calb
Producer	Shenzen Sinopoly Battery Co. Ltd.	China Aviation Lithium Battery Co. Ltd. (Calb)
Model	SP-LFP180AhA	CA180FI
Delivery date	Feb. 2017	Nov. 2018
Nominal capacity [Ah]	180	180
Nominal voltage [V]	3.2	3.2
Voltage range [V]	2.8–3.8	2.5–3.65
Maximum discharge C-rate [C]	3	2
Nominal weight [kg]	5.7	5.7
Size [mm^3]	282 × 182 × 71	280 × 180 × 71
Nominal energy [Wh]	576	576
Nominal specific density [$Wh\,kg^{-1}$]	101	101

(thermocouple Type K with Biologic and Pt100 with Basytec). Every cell, as delivered, was subjected to an initial characterization, which consisted of capacity tests, internal resistance (IR), and electrochemical impedance spectroscopy (EIS) measurements performed at 20 °C. Capacity tests were performed with 45 A (0.25 C) using a constant current constant voltage (CCCV) (CV phase cutoff current 0.02 C = 3.6 A) charge and CC discharge protocol for Sinopoly cells, and with 50 A (0.28 C) using a CCCV (CV phase cutoff current 0.05 C = 9 A) charge and discharge protocol for Calb cells.

For each cell type, two individual cells were selected for a detailed characterization. On these cells, rate capability tests were performed at 0.05 C (9 A), 0.25 C (45 A), and 0.83 C (150 A) current rates for Sinopoly cells with CCCV charge (CV phase cutoff current 0.02 C = 3.6 A) and CC discharge protocol, and at 0.1 C (18 A), 0.28 C (50 A), and 1 C (180 A) current rates for Calb cells with CCCV charge and discharge protocol (CV phase cutoff

current 0.05 C = 9 A). All tests were repeated at three different ambient temperatures: 5, 20, and 35 °C. The two selected cells showed the same voltage behavior and capacity within <2%, therefore only one data set will be shown later. In addition, for each cell type, a quasi-OCV (open-circuit voltage) curve was determined at 20 °C ambient temperature by measuring charge and discharge curves at very low (0.01 C for Sinopoly and 0.02 C for Calb) constant current, and taking the average voltage between the charge and discharge branches.

All C-rates reported in this article are given with respect to the nominal capacity C_N, not the real capacity, according to

$$C-\text{rate} = \frac{I \cdot 1\,\text{h}}{C_N} \tag{1}$$

where I is the current. State of charge (SOC) is defined by remaining cell capacity with the respect to the real cell capacity, according to

$$\text{SOC}\,(\%) = \frac{Q}{C_R} \times 100 \tag{2}$$

where Q is the measured charge throughput with respect to a fully discharged cell and C_R is the actual measured full capacity of the cell.

2.3. Structural and Morphological Characterization

For structural and morphological characterization, one cell of each type was opened in a glove box (MBraun Unilab Pro SP) under Argon atmosphere ($H_2O < 1$ ppm, $O_2 < 1$ ppm). For safety reasons, cells were discharged to their discharge cutoff voltages (CCCV: 0.1 C CC phase followed by 48 h CV phase) before opening. The cells were opened using either a specifically designed cutter (Treichel Engineering) and/or an oscillating tool (Fein). Structural characterization of the internal geometry was performed on each cell after manually disassembling the electrode stacks. The total active electrode area was measured with a ruler (resolution 1 mm), the thickness of the anode, cathode, separator, and current collector sheets where measured with a thickness dial gauge (Hahn und Kolb, resolution 1 µm), and the components were weighed by a precision balance (RADWAG PS600.X2, resolution 0.001 g).

For morphological characterization of the electrode microstructure, samples ($\approx 6 \times 5\,\text{cm}^2$) were cut out of the electrode sheets and washed three times. Each washing step took 2 h by immersing the sample in a clean petri dish filled by dimethyl carbonate (anhydrous, ≥99%, Sigma-Aldrich). The samples were flipped in the middle of the process to ensure homogeneity. Then the electrodes were dried overnight. For each electrode of each cell type, samples were investigated by light microscopy (Leica, DML2700 M) and by SEM (JEOL JSM-6610LV). For cross-sectional microscopy, samples ($\approx 1\,\text{cm}^2$) were prepared by cold mounting (Epofix, Struers) and then polished (Struers, Tegramin 20). The polishing protocol is shown in **Table 2**. For chemical characterization, the SEM samples were also investigated by EDX (Oxford Instruments X-Max).

Table 2. Polishing protocol of electrode samples.

Step	Disc	Medium	Contact pressure [N]	Duration [min]
Rough grinding	MD-Piano 220	Water	40	20
Fine grinding	MD-Largo	DiaPro Dac 9	20	20
Diamond polishing	MD-Dac	DiaPro Dac 3	20	15
Oxide polishing	MD-Chem	OP-s NonDry	20	5

2.4. Electrode Balance Analysis

The "balance" of the positive and negative electrodes refers to the range of lithium stoichiometries (x in Li_xC_6 for graphite, y in Li_yFePO_4 for LFP) that the cell uses during cycling between the cutoff voltages. We have developed and presented before a methodology to determine the balance from measured quasi- OCV data.[21] Briefly, measured half-cell potential curves (i.e., voltage of the active material operated vs lithium metal as function of lithium stoichiometry) for the two active materials (positive and negative) are taken from the literature. Using mathematical optimization, the stoichiometry ranges are determined by comparing full-cell voltage curves (i.e., cell voltage as function of charge throughput) synthesized from the half-cell curves to those measured from the target cell. The optimization and evaluation was conducted with a MATLAB-based tool.[21]

3. Results and Discussion

3.1. Electrical Characterization

For initial characterization of the as-delivered cells, the discharge/charge behavior of a total of 28 cells of each type was investigated. The measurement results in the form of cell voltage as function of charge throughput are shown in **Figure 2**. In this representation, the lower curves represent discharge, progressing in time from left to right; while the upper curves represent charge, progressing in time from right to left. Here and in the following figures and tables, the left column shows results from the Sinopoly cells, while the right column shows results from the Calb cells. Although both cell types have the same chemistry, their cutoff voltages, as specified by the manufacturer, are significantly different (cf. Table 1), leading to different curve shapes as obvious from Figure 2. For each type, the 28 individual cells show a strong scatter in their measured capacity. For Sinopoly, CC discharge capacities range from 158.9 to 195.8 Ah with an average of 169.5 Ah and a standard deviation of 11.9 Ah. For Calb, the scatter is less pronounced, with CC discharge capacities ranging from 188.9 to 199.2 Ah with an average of 195.9 Ah and a standard deviation of 2.4 Ah. Notably, for Calb, all cells have capacities above the nominal capacity (180 Ah), which is not the case for Sinopoly. The reason for the large scatter of the Sinopoly cells is unclear. Starting with the delivery date, all cells were stored and treated in-house in the same way; the scatter must therefore be assigned either to production itself (e.g., different production batches) or to cell history between production and delivery, which is unknown to us.

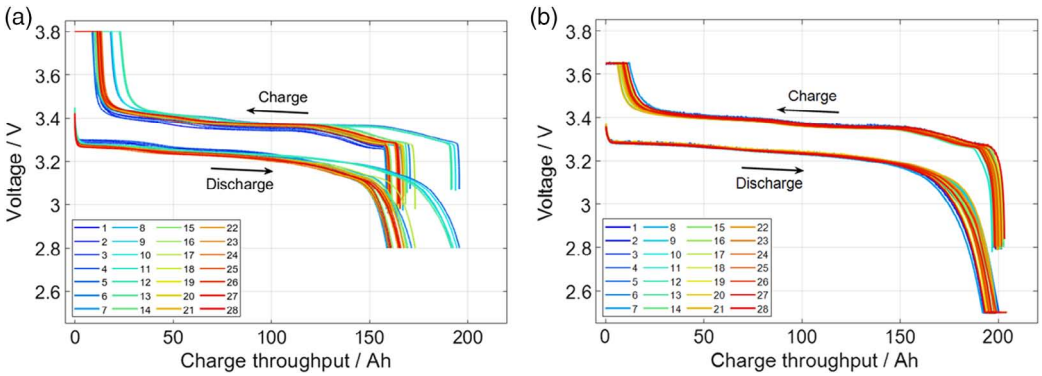

Figure 2. Discharge/charge curves of a) 28 Sinopoly cells and b) 28 Calb cells. The conditions were 0.25 C for Sinopoly and 0.28 C for Calb at 20 °C ambient temperature. The lower branches represent discharge (time progresses from left to right), while the upper branches represent charge (time progresses from right to left). The charge throughput (*x* scale) is defined as zero for a fully charged cell.

The scatter of the cell capacity is in both cases significant. When cells are integrated in systems, they are typically connected in series to increase voltage to a level suitable for inverters. The capacity scatter leads to a permanent debalancing of the cells in the system, potentially leading to accelerated aging, and posing a challenge to balancing systems. These effects are investigated in a parallel study.[22]

To further understand the cell electrical behavior, one cell of each type with typical capacity (Sinopoly 28, 164.9 Ah, and Calb 6, 195.6 Ah) was selected for a detailed characterization, which consisted of C-rate tests (recording of discharge/charge curves at different currents) at different ambient temperatures (5, 20, 35 °C). The results of this study are shown in **Figure 3**. Here, the same representation is used as in Figure 2, that is, cell voltage is plotted as function of charge throughput. The lower branches represent discharge and the upper branches charge. This representation has the advantage that overpotentials are easily visualized. This is indicated by the labels in panel (a). The overpotential η is defined[24,25] as the difference between operation voltage V and equilibrium voltage V^{eq}

$$\eta = V - V^{\mathrm{eq}} \tag{3}$$

The overpotential is (per this definition) negative for battery discharge (where $V < V^{\mathrm{eq}}$) and positive for battery charge (where $V > V^{\mathrm{eq}}$). An increasing gap between discharge and charge branches means increasing overpotentials.

As shown in Figure 3, both cells, Sinopoly (left) and Calb (right), show qualitatively the same behavior, which can be summarized as follows. 1) An increase in the C-rate leads to increased overpotentials, as visible in the increasing gap between discharge and charge branches. This is a typical behavior of electrochemical cells and is due to increasing ohmic, electrochemical, and transport losses.[24,25] 2) As consequence of the increased overpotential, an increase in the C-rate leads to a decrease in the CC-dischargeable capacity. This is referred to as "capacity-rate effect."[26] However, for the relatively low currents investigated here ($\leq$ 1 C), the effect is small, compared with other cell types.[27] 3) Increasing temperature has a similar effect as decreasing the C-rate, both on capacity and overpotential. As a result, using the Calb cell as example, 5 °C/0.1 C shows a very similar curve as 35 °C/1 C. 4) The overpotentials show an asymmetric behavior with respect to charge and discharge: upon discharge, overpotentials increase toward low SOC, while upon charge, overpotentials increase toward high SOC. This asymmetry is indicated by the arrows in panel (a). It is pronounced for low temperatures and high C-rates. A similar asymmetry has been observed in cells with NCA cathode,[28] although the mechanism may be different in the present LFP cells.

It is interesting to study heat losses during cycling, both because they affect system-level thermal management strategies and because they lower the energy efficiency. **Figure 4** shows measured temperature differences, defined as

$$\Delta T(t) = T_{\mathrm{cell}}(t) - T_{\mathrm{ambient}} \tag{4}$$

as function of time for different C-rates and ambient temperatures. The cell temperature, T_{cell}, is measured at the cell surface with a thermocouple. The ambient temperature, T_{ambient}, is the set point of the climate chamber. During cycling, the increase in cell temperature relative to the ambient depends on C-rate and ambient temperature itself. It shows a distinct temporal behavior which is due to a combination of irreversible and reversible heating. The heating power $\dot{Q}$ within an electrochemical cell is given as[29]

$$\dot{Q} = -I \cdot \eta - I \cdot (T - T^0) \cdot \frac{\mathrm{d}V^{\mathrm{eq}}}{\mathrm{d}T} \tag{5}$$

where the first term on the right-hand side represents irreversible heating (always positive) and the second term reversible (entropic) heating (positive or negative, depending signs of current and $\mathrm{d}V^{\mathrm{eq}}/\mathrm{d}T$). The overpotentials η are highest at low temperatures (cf. Figure 3), causing high irreversible heating (first term). Therefore, the largest ΔT are observed at low ambient temperatures of 5 °C, and ΔT is generally lowest at ambient temperatures of 35 °C. At low currents, the contribution of the reversible heating can become important, causing nonmonotonous temperature curves. Note that, in particular at low currents, ΔT is well below 1 °C and the measurements may additionally be influenced by small fluctuations in the ambient temperature.

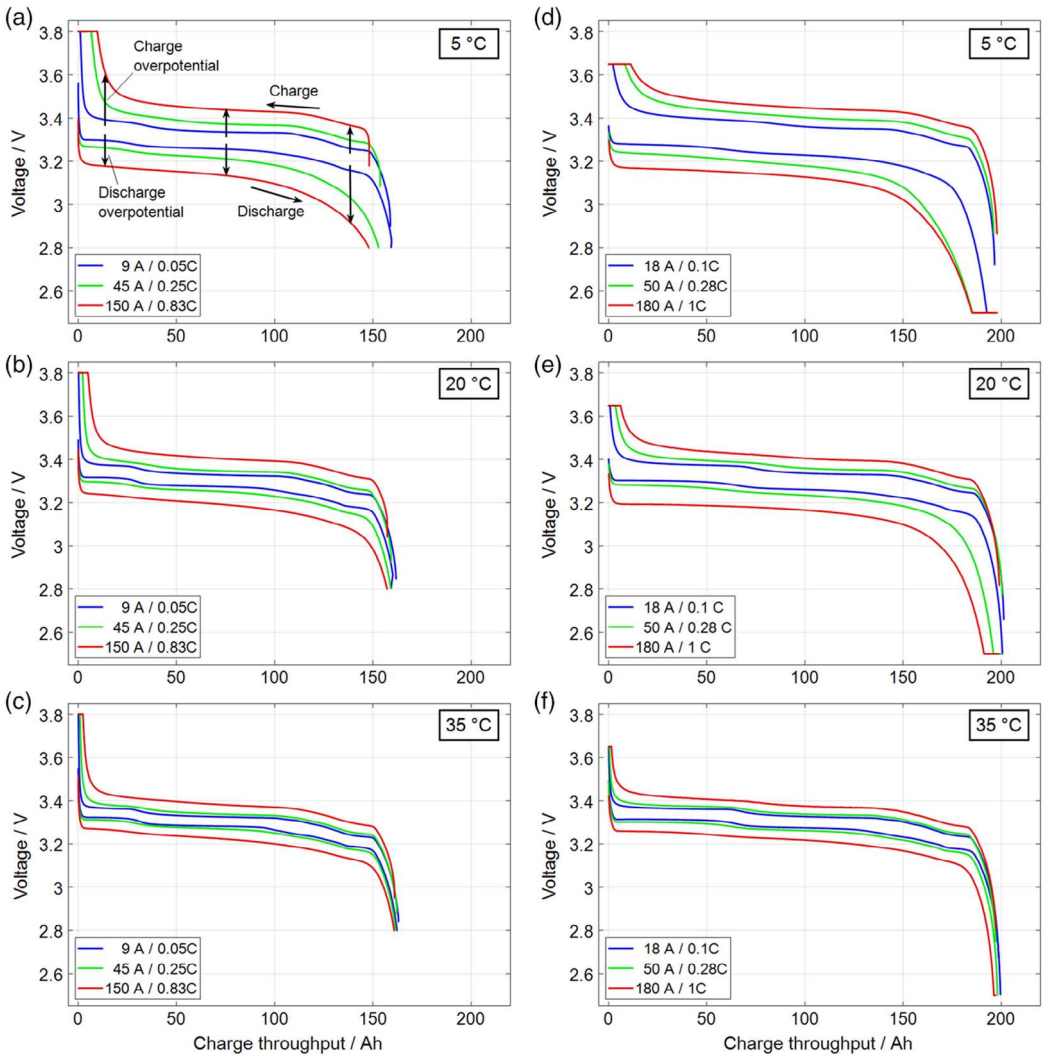

Figure 3. Discharge/charge curves of a–c) Sinopoly and d–f) Calb cells at three different ambient temperatures (5, 20, 35 °C). The lower branches represent discharge (time progresses from left to right), while the upper branches represent charge (time progresses from right to left). The charge throughput (x scale) is defined as zero for a fully charged cell.

The energy efficiency η_{en} of the cells is shown in **Figure 5**. It is defined and determined as

$$\eta_{en} = \frac{E_{discharge}}{E_{charge}} = \frac{\int_{discharge} I(t)V(t)dt}{\int_{charge} I(t)V(t)dt} \tag{6}$$

Both cell types show high efficiencies above 88% for all investigated conditions, reaching up to almost 99% for the Calb cell at 35 °C. The efficiency of the Sinopoly cell shows considerably less dependency on ambient temperature than that of the Calb cell. At low temperature (5 °C), therefore, the efficiency is higher for the Sinopoly cell. As efficiencies below unity are due to irreversible heat losses, η_{en} is indirectly related to the cell temperature increase: conditions with observed high ΔT (Figure 4: low ambient temperature and/or high C-rate) were also observed to have low η_{en} (Figure 5).

3.2. Internal Geometry

One cell of each type was opened to assess the internal design as well as to take samples for microscopy analyses. For Calb, this was a fresh cell (as delivered). For Sinopoly, lacking availability of fresh cells at the time of experiment, this was a cell that had undergone full cycling (897 cycles at 150 A over a period of 2 years) down to a state of health (remaining capacity) of 89.6%. Pictures of the cells after cutting and removing the lower part of the casing are shown in **Figure 6**. Both cell types have a similar internal design. Each cell consists of two electrode stacks which are separately wrapped in a plastic foil and taped together. The current collector tabs are connected to the outer terminals. Both cells have a pressure vent, but no positive temperature coefficient (PTC) connector or other safety features could be identified. For further disassembly, the current collector tabs were cut and the stacks were unwrapped. For each stack, a

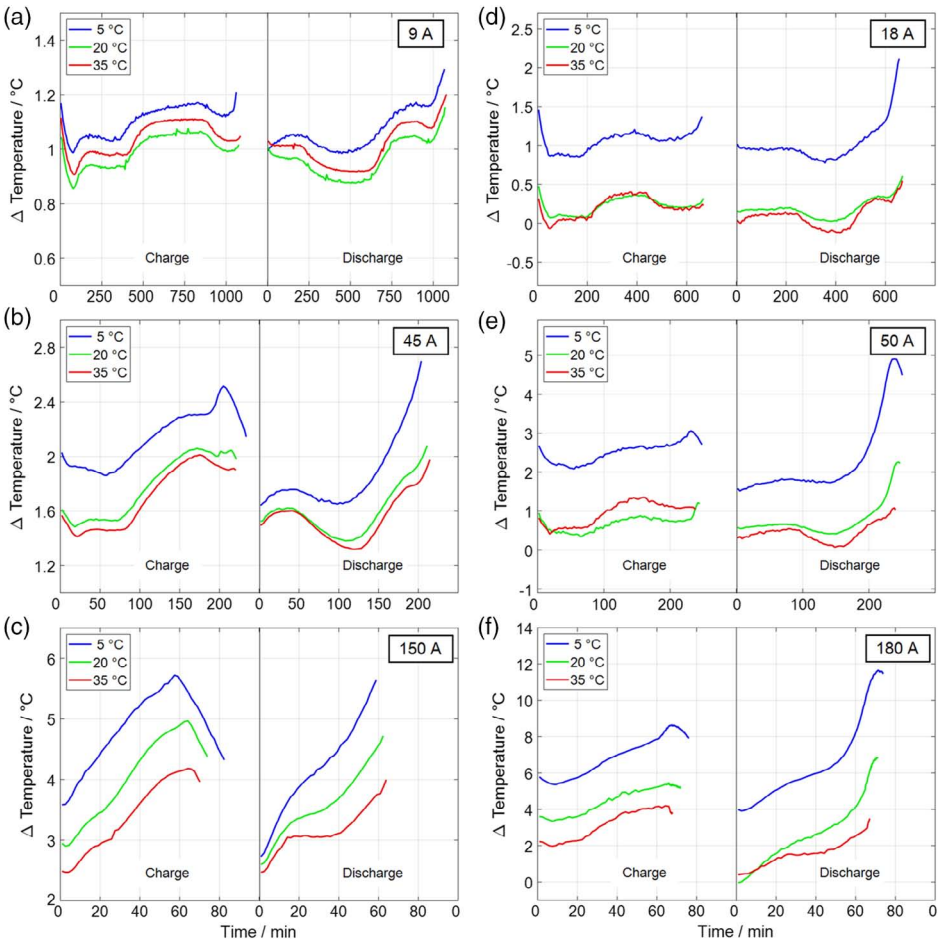

Figure 4. Difference between cell surface temperature and ambient temperature as function of time for a–c) Sinopoly and d–f) Calb cells at different C-rates and different ambient temperatures, as given in the legends.

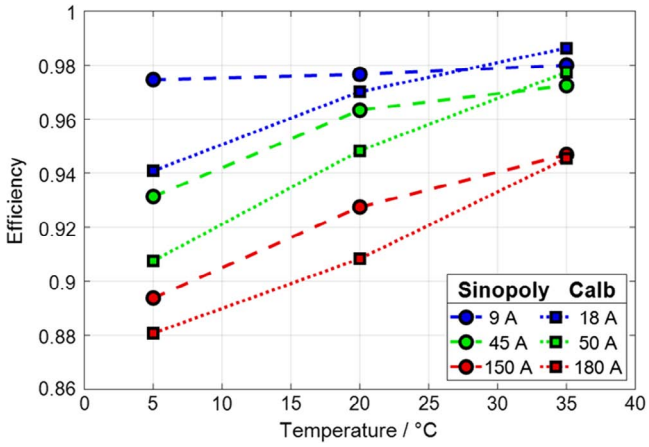

Figure 5. Discharge/charge energy efficiency of Sinopoly (circles) and Calb (squares) cells at three different temperatures (5, 20, 35 °C).

single long separator sheet was observed to be arranged in Z form between the stacked electrode sheets (no winding). Here and in the following, we use the term "electrode sheet" for a current collector foil coated on both sides with electrodes. All electrode sheets, including the outermost, were double-side coated. Pictures of the sheets are shown in **Figure 7**. The electrode and separator sheets of the (aged) Sinopoly cell qualitatively appear more used than those of the (fresh) Calb cell.

Details of the geometrical and weight properties of all components are shown in **Table 3**. Both cells show a similar, but not identical design. Both cells contain 146 negative and 144 positive electrode sheets (counting both stacks). There is a clear anode overhang,[30] the anode having a larger area than the cathode by 4.9% (Sinopoly) and 5.7% (Calb).

The mass distribution of the cell components is shown in **Figure 8**. In both cell types, the positive electrode is the dominating component, providing around one-third of the whole cell mass, followed by the casing (around one-quarter) and the negative electrode (around one-fifth of the cell mass). The large contribution of the casing is remarkable. Both cells have a full-plastic hard case with significant thicknesses of 5.3 mm (Sinopoly) and 6.2 mm (Calb). The manufacturers seem to accept the lowered specific energy resulting from the massive housing at the benefit of high mechanical stability.

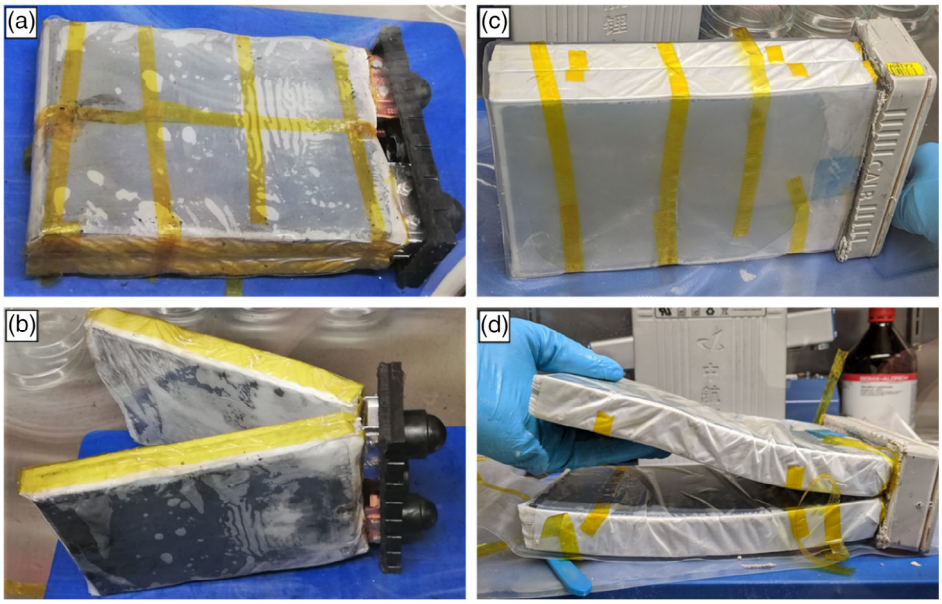

Figure 6. Pictures of the cells in the glove box after opening, showing the internal design of a,b) Sinopoly and c,d) Calb cells.

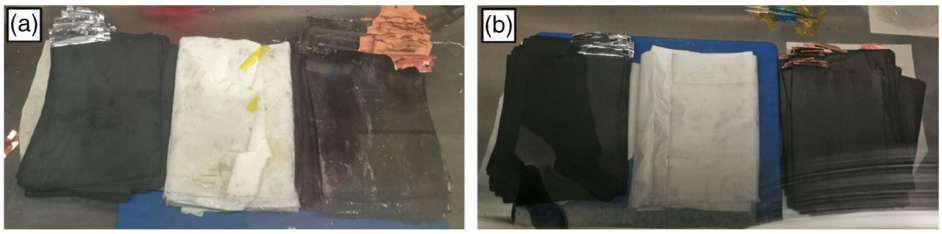

Figure 7. Positive electrode sheets (left), separator sheet (middle), and negative electrode sheets (right) of a) Sinopoly and b) Calb cells.

Table 3. Internal geometrical properties and component masses of the two cell types.

	Sinopoly			Calb		
	Negative electrode	Separator	Positive electrode	Negative electrode	Separator	Positive electrode
Height [cm]	22.0	23.9	21.5	22.5	23.5	22.0
Width [cm]	15.9	2382	15.4	15.7	2431	15.3
Thickness (single sheet) [μm]	128.8	44.1	178.7	140.7	31.6	176.6
Thickness (single current collector) [μm]	15.3	–	26.1	15.6	–	25.6
Thickness (single electrode) [μm]	56.8	–	76.3	62.6	–	75.5
Area (single sheet) [cm^2]	348.0	384.8	329.3	350.5	379.5	334.1
Volume (single sheet) [cm^3]	4.48	1.69	5.89	4.93	1.12	5.90
Number of sheets	146	2	144	146	2	144
Total area [m^2]	10.16	11.39	9.485	10.24	11.43	9.623
Total volume [cm^3]	654.4	502.3	847.5	720.3	361.1	849.9
Total mass electrodes [g]	906	–	1644	1190	–	1907
Mass loading electrodes [$mg\,cm^{-2}$]	8.92	–	17.3	11.6	–	19.8
Total mass (sheet) [g]	1560	369.2	1997	1331	308.5	1976
Total mass current collection[a)] [g]	654	–	353	141	–	69

[a)]Includes the aluminum and copper foils, tab collectors, and terminals.

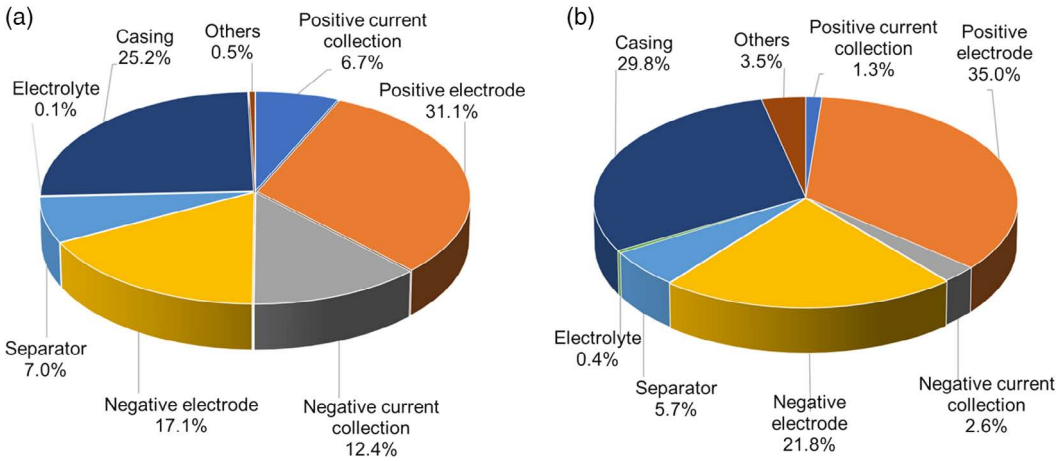

Figure 8. Mass distribution of the components of a) Sinopoly and b) Calb cells. "Electrolyte" refers to the free liquid that was left inside the casing after removing the electrode stacks (electrolyte soaked in the porous electrodes could not be measured). "Current collection" includes the metal foils, tab collectors, and terminals. "Others" refers to plastic foils and tapes wrapped around the electrode stacks, screws of the tab collection system, and seals.

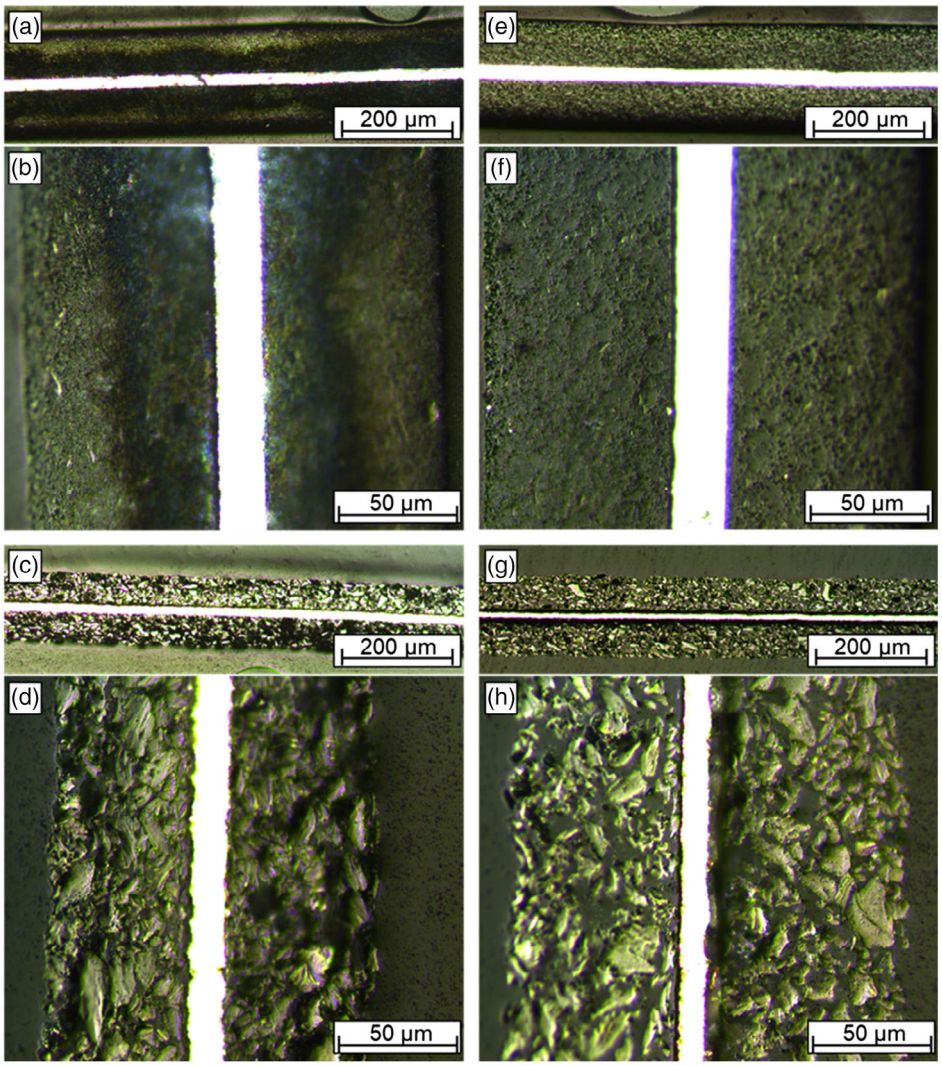

Figure 9. Light microscopy investigations of polished electrodes (cross section): a,b) Sinopoly positive electrode and c,d) negative electrode, e,f) Calb positive electrode, and g,h) negative electrode. Close to the upper border of panels (a) and (e) sample holders are visible.

3.3. Electrode Microstructure

To characterize the electrode microstructure, both electrode sheets of both cell types were investigated via light microscopy (providing a lower resolution overview) and SEM (providing high-resolution results and allowing chemical analysis via EDX). Results of the light microscopy are shown in **Figure 9**. All samples were investigated in cross-sectional view (cf. Section 2.3 for sample preparation). The left images (panels a–d) show results from the Sinopoly cell, the right images (panels e–h) from the Calb cell, and each electrode is shown both with lower and with higher resolution. All micrographs show the current collector in the center as bright bar, coated on both sides with the porous composite electrodes. The positive electrodes (upper part of Figure 9) have a compact appearance—a granular structure may be present; however, it seems to be below the resolution limit of the light microscope. The negative electrodes (lower part) show a clear composite appearance with granular features in the 5–10 μm range. The thicknesses for the Sinopoly cell are 176 μm for the positive

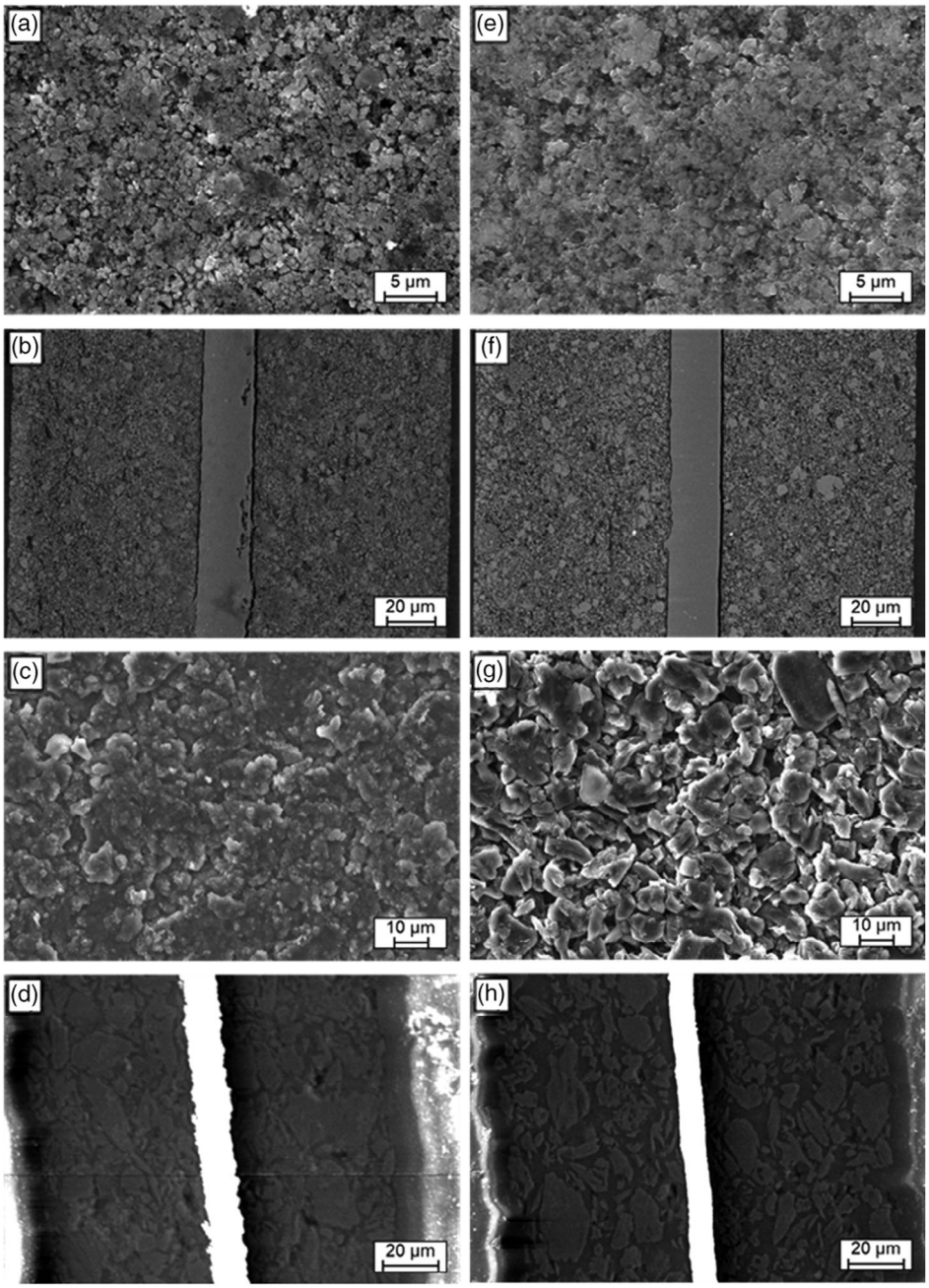

Figure 10. Scanning electron microscopy investigation: Sinopoly positive electrode in a) top view and b) cross-sectional view, c) negative electrode in top view, and d) cross-sectional view; Calb positive electrode in e) top view and f) cross-sectional view, g) negative electrode in top view, and h) cross-sectional view.

electrode sheet and 126 μm for the negative electrode sheet. The thicknesses for the Calb cell are 178 μm for the positive electrode sheet and 137 μm for the negative electrode sheet. The thickness values measured from the light microscopy are consistent with the ones measured by thickness gauge within <15% deviation (cf. Table 3). The samples might be larger due to the absence of applied pressure by thickness gauge and removal of electrolyte during washing procedure of the samples.

Electron micrographs are shown in **Figure 10**. Here, each electrode is shown both in top view (sample preparation only by washing) and in cross-sectional view. For the positive electrodes (upper images), the granular structure of the electrode is clearly visible—SEM provides a significantly better resolution than light microscopy. The top views (a,e) show irregularly shaped but roughly spherical particles that are in 0.4 μm diameter range for the Sinopoly and in the 0.5 μm diameter range for the Calb cell. In the Calb cell (e), the particles appear more densely packed and agglomerated than in the Sinopoly cell (a). The cross-sectional views (b,f) show a combination of fine and occasional larger particles. The electrodes seem to have slightly detached from the right side of the current collector, probably a consequence of sample preparation. For the negative electrodes (lower images), the top views (c,g) reveal irregularly shaped, flake-like particles that are in 10 μm diameter range for the Sinopoly and in the 15 μm diameter range for the Calb cell. The cross-sectional view (d,h) does not provide a very good contrast between the active material particles and the resin-filled porosity. Still, the irregularity of the particle shapes and a significant size distribution is obvious for both cell types. The Sinopoly electrode (d) seems closer packed with smaller porosity than the Calb electrode (h). The thicknesses measured from the cross-sectional views of Sinopoly cell are 182 μm for the positive electrode sheet and 128 μm for the negative electrode sheet. The thicknesses measured from the cross-sectional views of Calb cell are 181 μm for the positive electrode sheet and 139 μm for the negative electrode sheet. The thickness values are consistent with those determined by light microscopy.

Table 4. Results of EDX analysis. All values in percent. Missing values mean below detection limit.

	Sinopoly positive electrode	Sinopoly negative electrode	Calb positive electrode	Calb negative electrode
Iron, Fe	26.74	–	26.12	–
Phosphorus, P	14.73	1.23	13.47	0.18
Oxygen, O	35.17	18.24	36.65	6.02
Aluminum, Al	–	0.02	–	–
Carbon, C	19.92	58.25	23.07	89.18
Cadmium, Cd	–	0.01	–	–
Copper, Cu	–	1.05	–	1.11
Fluorine, F	2.99	20.62	–	3.31
Silicon, Si	0.03	0.23	–	0.19
Sodium, Na	–	–	–	0.03
Sulfur, S	0.20	0.36	–	–
Cobalt, Co	–	–	0.03	–
Vanadium, V	0.24	–	–	–
Iridium, Ir	–	–	0.44	–
Titanium, Ti	–	–	0.21	–
Yttrium, Y	–	–	–	–
Identified material	LFP	Graphite	LFP	Graphite

EDX was used to probe the chemical composition of the electrodes. The top-view samples were used. The results are shown in **Table 4** for all four investigated electrodes. The results allow to clearly identify LFP and graphite as active materials in both cell types, as those elements (Fe, P, O at the positive and C at the negative electrodes) are the majority species identified in the EDX signal. Both positive electrodes also show a significant amount of carbon, which is typically used as conductive additive in LFP electrodes.[31,32] Both Sinopoly electrodes also show a non-negligible fluorine signals, probably solid electrolyte interphase (SEI) components originating from electrolyte degradation[33]—note that these electrodes were harvested from an aged cell. Consequently, the (fresh) Calb cell shows no fluorine at the positive and only little at the negative electrode. The oxygen observed at both negative electrodes may similarly result from SEI components. The remaining elements shown in Table 4 are negligible or below detection limits. In particular, no sign of other, blended active materials (such as silicon at the negative electrodes or cobalt at the positive electrodes) could be identified. Notably, no yttrium was found, despite the claim of the Sinopoly data sheet to use $LiFeYPO_4$. The data such confirm that the chemistry of both cell types is LFP/graphite.

Overall, the combined light microscopy, SEM, and EDX investigations show that both cell types have similar, but not identical electrode properties in terms of particle size and shape, electrode morphology, and materials chemistry.

3.4. Electrode Balances

As final step of the present analysis, we determined the lithium stoichiometries the electrodes of the two cell types are operated in. To this goal, we used an optimization tool developed and presented before.[21] Main input is the molar enthalpies and entropies of intercalated lithium as function of stoichiometry for the two active materials. These data were derived from literature experiments as described by Mayur et al.,[34] using half-cell potential curves (voltage of the active material operated vs lithium metal as function of lithium stoichiometry) and their temperature dependence. Many different studies are available for LFP and graphite, and we obtained the best optimization results with the following data. For LFP, half-cell potential curves were taken from Verbrugge et al.,[35] and entropies from Viswanathan et al.[36] For graphite, half-cell potential curves were taken from Smekens et al.,[37] and entropies from Reynier et al.[38]

Results of the analysis are shown in **Figure 11**, where again the left and right panels correspond to Sinopoly and Calb cells, respectively. Panels (a) and (e) show measured quasi-stationary (C/100 for Sinopoly cell, C/50 for Calb cell) charge/discharge curves, their average, and the synthetic curves after optimization. For both cell types, the simulation matches very well with the

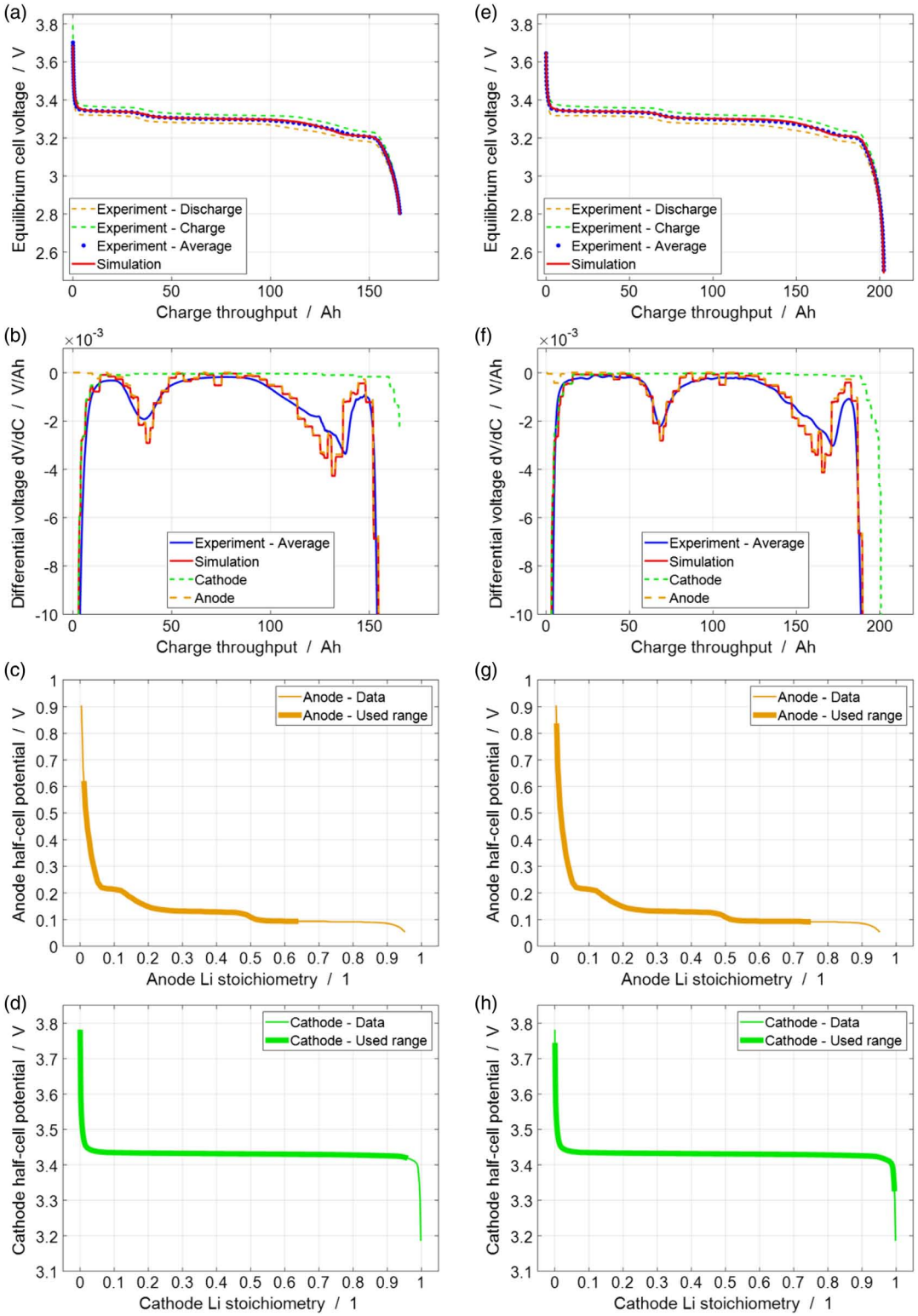

Figure 11. Results of the electrode balancing analysis of Sinopoly (left) and Calb (right) cells: a,e) quasi-OCV curves, b,f) differential voltage curves, c,g) negative electrode half-cell voltage, and d,h) positive electrode half-cell voltage.

experimental data. This is confirmed in the differential voltage analysis shown in panels (b) and (f). The small but characteristic steps in the voltage curves are well reproduced by the simulation. For the two cell types, they appear at different charge

Table 5. Self-consistent parameter set of the two cell types.

	Sinopoly		Calb	
	Negative electrode	Positive electrode	Negative electrode	Positive electrode
Active material	Graphite	LFP	Graphite	LFP
Density [kg m^{-3}]	2270[43]	3600[44]	2270[43]	3600[44]
Molar mass [g mol^{-1}]	72.1	150.8	72.1	150.8
Half-cell thermodynamic data	[35,36](cf. Figure 11c)	[37,38](cf. Figure 11d)	[35,36](cf. Figure 11c)	[37,38](cf. Figure 11d)
Active electrode area [m^2]	9.48		9.62	
Electrode thickness [m]	56.7×10^{-6}	76.3×10^{-6}	62.6×10^{-6}	75.5×10^{-6}
Capacity [Ah]	165		202	
Volume fraction at 50% SOC	0.597	0.381	0.554	0.448
Lithium stoichiometry range	0.011 ... 0.64	1.9×10^{-5} ... 0.96	0.005 ... 0.75	0.0004 ... 0.995
Active material loading [mg cm^{-2}]	7.68	10.5	7.87	12.2
Active material capacity [mAh cm^{-2}]	2.72	1.81	2.82	2.11
Used electrode capacity [mAh cm^{-2}]	1.74		2.10	

throughputs—a clear sign of the differing anode balance. As shown from the deconvolution presented as dashed lines in panels (b) and (f), these steps can be fully assigned to the graphite anode, while the LFP cathode dominates the curve only at very low charge throughput. Panels (c) and (g) show the graphite anode half-cell potential curves. The literature input is shown as thin line, while the stoichiometry range used in the cells during cycling is included as bold line. The two cell types show a clearly different behavior, with the Sinopoly cell (panel c) showing a smaller stoichiometry range than the Calb cell (panel g). Finally, panels (d) and (h) show the same representation for the LFP cathode. The complete plateau range and in fact almost the complete stoichiometry range are used for cycling.

The quantitative results of the electrode balance analysis are shown in **Table 5**. This table also includes the required input parameters. When electrode areas and thicknesses are known, as in the current study, the optimization output includes the volume fraction of active material in the electrodes. These data are also shown in Table 5. Taken as a whole, the table provides a complete and self-consistent data set of chemical and structural parameters of the two cell types. These parameters provide the basis for future modeling and simulation investigations, both physicochemical continuum models (so-called pseudo-2D, P2D, or Newman-type models)[17,39] and semiempirical equivalent circuit (EC) models.[20]

From the point of view of cell manufacturing, it is interesting to quantify the loading of active materials. The electrode balance analysis allows to deduce the area-specific active material loading m^A_{AM} (in mg cm^{-2}) as

$$m^A_{\mathrm{AM}} = \frac{m_{\mathrm{AM}}}{A_{\mathrm{e}}} = \frac{V_{\mathrm{AM}} \cdot \rho_{\mathrm{AM}}}{A_{\mathrm{e}}} = \frac{V_{\mathrm{e}} \cdot \varepsilon_{\mathrm{AM}} \cdot \rho_{\mathrm{AM}}}{A_{\mathrm{e}}} = d_{\mathrm{e}} \cdot \varepsilon_{\mathrm{AM}} \cdot \rho_{\mathrm{AM}} \tag{7}$$

the usable electrode capacity C^A (in mAh cm^{-2}) as

$$C^A = \frac{C_{\mathrm{cell}}}{A_{\mathrm{e}}} \tag{8}$$

and the areal capacity C^A_{AM} (in mAh cm^{-2}) as

$$C^A_{\mathrm{AM}} = \frac{C^A}{\Delta X_{\mathrm{Li}}} \tag{9}$$

In these equations, AM stands for active material (graphite or LFP), m_{AM} is the total active material mass in the cell, A_{e} is the active electrode area, V_{AM} is the total volume of active material, ρ_{AM} is the density, V_{e} is the electrode volume, d_{e} is the electrode thickness, $\varepsilon_{\mathrm{AM}}$ is the volume fraction, C_{cell} is the cell capacity, and ΔX_{Li} is the lithium stoichiometry range during cycling. The resulting values are shown in Table 5. The areal capacities are in the range of 1.8–2.8 mAh cm^{-2} and therefore lower than the values of 3–4 mAh cm^{-2} that Lin et al.[40] reported for "current" lithium-ion batteries. The active materials mass loadings are in the range of 7.7–12.2 mg cm^{-2}, which is less than the measured total mass loadings of 8.9–19.8 mg cm^{-2} (cf. Table 3), indicating the significant contribution of inactive materials such as binder and conductive additives to the electrode mass.

4. Conclusions

In this study, we have presented the detailed electrical, thermal, structural, and chemical characterization of 180 Ah LFP/graphite prismatic cells from two different manufacturers (Sinopoly, Calb) used in home-storage systems. The main results can be summarized as follows: 1) The 28 individual cells of each type show a significant capacity scatter, which is particularly pronounced in case of the Sinopoly cell. This scatter is problematic if the cells are used in serially connected battery pack configurations, where the use of balancing units will be required. 2) The electrical performance of the two cell types is similar. The charge/discharge characteristics show a weak capacity-rate effect (for investigated C-rates up to 1 C) and a strong dependence on temperature (for investigated temperatures between 5 and 35 °C). This is a typical behavior for lithium-ion cells. 3) Both cells have a high electrical energy efficiency above 90% of the

discharge/charge cycle. The efficiency increases with increasing temperature and decreasing C-rate, with measured values up to 98% for 35 °C/C/10 cycles. This excellent efficiency makes the cells well suited for renewable energy storage applications. 4) The internal cell designs, analyzed after cell opening under Argon atmosphere, consist of two electrode stacks with a total of 144 positive and 146 negative electrode sheets. It is remarkable that the electrode sheets are stacked, as would be rather typical for pouch cells, and not wound in a jelly roll, as is considered typical for prismatic cells.[41] 5) The nominal specific energy of the cells is 101 Wh kg^{-1}, which is low compared with other high-energy lithium-ion cells. For both cells, the massive casing (6.2 mm for the Calb cell) has a large contribution (approximately one quarter) to the total weight. As the target application of the cells is stationary energy storage, the low specific energy is not problematic. 6) The electrode morphologies, as investigated with light microscopy and SEM, show small, submicrometer particles for LFP and large, 10 μm scale irregularly shaped particles for graphite. Electrode balance analysis reveals LFP volume fractions of 38.1% and 44.8%, and graphite volume fractions of 59.7% and 55.4% for the Sinopoly and Calb cells, respectively. The LFP volume fractions are rather low. 7) Chemical analysis with EDX confirmed the LFP/graphite cell chemistry. The positive electrodes contain significant amounts of carbon as conductive additive. This is consistent with the observed low LFP volume fractions, which contributes to the overall low specific energy. 8) The electrode balances were determined with a mathematical optimization algorithm. The negative electrodes are cycled to lithium stoichiometries up to 64% and 75% for the Sinopoly and Calb cells, respectively. The difference is not only a consequence of different electrode loading, but also related to the significantly different cutoff voltages specified by the manufacturers. A significant part (1/3–1/4) of the graphite capacity is therefore unused. Furthermore, the two cell types show an anode overhang[30] of 4.9% and 5.7%, respectively. Both, reduced cycling stoichiometry and anode overhang, are known strategies to reduce plating propensity and therefore increase cell lifetime.[41,42] 9) The combined empirical data and mathematical analysis resulted in a complete and self-consistent parameter set of the two cell types. These parameters are requirements for follow-up modeling and simulation studies of these cells, both physicochemical models and equivalent circuit models.

Overall, the two cell types show not only strong similarities concerning the electrical performance, internal design, and cell chemistry, but also differences in electrode morphology and balances. The investigation of their performance as part of home-storage systems, including aging characteristics, will be part of future studies.

Acknowledgements

The authors thank Pascale Müller (Offenburg University of Applied Sciences) for strongly supporting the microscopy investigations. The authors also thank Hanhee Kim (Offenburg University of Applied Sciences) for supporting the development of thermodynamic data of active materials. This work was partially funded by the German Ministry of Education and Research (BMBF) in the framework of the STABIL project (grant no. 03FH004PX5) and by the European Regional Development Fund and the Land Baden-Württemberg in the framework of the LIBlife project (grant no. FEIH_KMU_1098567). The work was partially conducted in the Enerlab 4.0 laboratory which was funded by the BMBF (grant no. 13FH091IN6).

Open access funding enabled and organized by Projekt DEAL.

Conflict of Interest

The authors declare no conflict of interest.

Data Availability Statement

Research data are not shared.

Keywords

energy storage, large format, lithium iron phosphate, lithium-ion batteries, performance characteristics

Received: October 16, 2020
Revised: January 31, 2021
Published online: March 23, 2021

[1] K.-P. Kairies, J. Figgener, D. Haberschusz, O. Wessels, B. Tepe, D. U. Sauer, *J. Energy Storage* **2019**, *23*, 416.
[2] J. Figgener, P. Stenzel, K.-P. Kairies, J. Linßen, D. Haberschusz, O. Wessels, G. Angenendt, M. Robinius, D. Stolten, D. U. Sauer, *J. Energy Storage* **2020**, *29*, 101153.
[3] V. Quaschning, *Regenerative Energiesysteme*, Carl-Hanser-Verlag, München, Germany **2015**.
[4] D. Geckeler, C. Payá Alemany, *Batteriespeicher: Der Leitfaden für Industrie- und Gewerbeanwendungen*, denersol, Berlin **2018**.
[5] H. Hesse, M. Schimpe, D. Kucevic, A. Jossen, *Energies* **2017**, *10*, 2107.
[6] L. Hoffmann, J.-K. Grathwol, W. Haselrieder, R. Leithoff, T. Jansen, K. Dilger, K. Dröder, A. Kwade, M. Kurrat, *Energy Technol.* **2020**, *8*, 1900196.
[7] M. Dubarry, B. Y. Liaw, M.-S. Chen, S.-S. Chyan, K.-C. Han, W.-T. Sie, S.-H. Wu, *J. Power Sources* **2011**, *196*, 3420.
[8] T. Grandjean, A. Barai, E. Hosseinzadeh, Y. Guo, A. McGordon, J. Marco, *J. Power Sources* **2017**, *359*, 215.
[9] K. Theinglim, P. Poramapojana, in *SAE Technical Paper Series*, SAE International400 Commonwealth Drive, Warrendale, PA **2019**.
[10] R. Youssef, J. He, M. Akbarzadeh, J. Jaguemont, L. D. Sutter, M. Berecibar, J. van Mierlo, in *2020 9th Int. Conf. on Renewable Energy Research and Application (ICRERA)*, IEEE, Piscataway, NJ **2020**, pp. 43–47.
[11] W. Shi, X. Hu, J. Wang, J. Jiang, Y. Zhang, T. Yip, *Electrochim. Acta* **2016**, *196*, 13.
[12] M. Ouyang, X. Feng, X. Han, L. Lu, Z. Li, X. He, *Appl. Energy* **2016**, *165*, 48.
[13] J. Li, Y. L. Song, *AMR* **2012**, *463–464*, 753.
[14] M. L. Bacci, F. Cheli, E. Sabbioni, D. Tarsitano, M. Vignati, in *2017 Int. Conf. of Electrical and Electronic Technologies for Automotive*, IEEE, Piscataway, NJ **2017**, pp. 1–6.
[15] S. Panchal, M. Rashid, F. Long, M. Mathew, R. Fraser, M. Fowler, in *SAE Technical Paper Series*, SAE International400 Commonwealth Drive, Warrendale, PA **2018**.
[16] *Green Energy and Technology* (Eds: A. A. Franco, M. L. Doublet, W. G. Bessler), Springer, London, Heidelberg, NY, Dordrecht **2016**.

[17] M. Doyle, T. F. Fuller, J. Newman, *J. Electrochem. Soc.* **1993**, *140*, 1526.
[18] Y. Merla, B. Wu, V. Yufit, R. F. Martinez-Botas, G. J. Offer, *J. Power Sources* **2018**, *384*, 66.
[19] S. De, P. W. C. Northrop, V. Ramadesigan, V. R. Subramanian, *J. Power Sources* **2013**, *227*, 161.
[20] A. Seaman, T.-S. Dao, J. McPhee, *J. Power Sources* **2014**, *256*, 410.
[21] M. Mayur, M. C. Yagci, S. Carelli, P. Margulies, D. Velten, W. G. Bessler, *Phys. Chem. Chem. Phys.* **2019**, *21*, 23672.
[22] M. C. Yagci, T. Feldmann, E. Bollin, W. G. Bessler, **2020**.
[23] J. Chen, X. Wang, Z. Ma, G. Shao, *Ionics* **2015**, *21*, 2701.
[24] P. W. Atkins, J. D. Paula, *Atkins' Physical Chemistry*, Oxford University Press, Oxford, Great Britain **2006**.
[25] J. Newman, K. E. Thomas-Alyea, *Electrochemical Systems*, John Wiley & Sons, Hoboken, NJ **2004**.
[26] T. Reddy, *Linden's Handbook of Batteries*, McGraw-Hill Education, New York, USA **2010**.
[27] F. Hall, J. Touzri, S. Wußler, H. Buqa, W. G. Bessler, *J. Energy Storage* **2018**, *17*, 109.
[28] F. Hall, S. Wußler, H. Buqa, W. G. Bessler, *J. Phys. Chem. C* **2016**, *120*, 23407.
[29] T. M. Bandhauer, S. Garimella, T. F. Fuller, *J. Electrochem. Soc.* **2011**, *158*, R1.
[30] J. P. Fath, L. Alsheimer, M. Storch, J. Stadler, J. Bandlow, S. Hahn, R. Riedel, T. Wetzel, *J. Energy Storage* **2020**, *29*, 101344.
[31] W.-J. Zhang, *J. Power Sources* **2011**, *196*, 2962.
[32] S. L. Bewlay, K. Konstantinov, G. X. Wang, S. X. Dou, H. K. Liu, *Mater. Lett.* **2004**, *58*, 1788.
[33] P. Verma, P. Maire, P. Novák, *Electrochim. Acta* **2010**, *55*, 6332.
[34] M. Mayur, S. C. DeCaluwe, B. L. Kee, W. G. Bessler, *Electrochim. Acta* **2019**, *323*, 134797.
[35] M. Verbrugge, D. Baker, B. Koch, X. Xiao, W. Gu, *J. Electrochem. Soc.* **2017**, *164*, E3243.
[36] V. V. Viswanathan, D. Choi, D. Wang, W. Xu, S. Towne, R. E. Williford, J.-G. Zhang, J. Liu, Z. Yang, *J. Power Sources* **2010**, *195*, 3720.
[37] J. Smekens, J. Paulsen, W. Yang, N. Omar, J. Deconinck, A. Hubin, J. van Mierlo, *Electrochim. Acta* **2015**, *174*, 615.
[38] Y. Reynier, R. Yazami, B. Fultz, *J. Power Sources* **2003**, *119–121*, 850.
[39] S. Carelli, M. Quarti, M. C. Yagci, W. G. Bessler, *J. Electrochem. Soc.* **2019**, *166*, A2990.
[40] Z. Lin, T. Liu, X. Ai, C. Liang, *Nat. Commun.* **2018**, *9*, 5262.
[41] R. Korthauer, *Handbook Lithium-Ion Batteries*, Springer, Berlin, Heidelberg **2018**.
[42] S. Carelli, W. G. Bessler, *J. Electrochem. Soc.* **2020**, *167*.
[43] W. M. Haynes, D. R. Lide, T. J. Bruno, *CRC Handbook of Chemistry and Physics. A Ready-Reference Book of Chemical and Physical Data: 2013-2014*, CRC Press, Boca Raton (FL)/London, NY **2013**.
[44] V. A. Streltsov, E. L. Belokoneva, V. G. Tsirelson, N. K. Hansen, *Acta Crystall. B* **1993**, *49*, 147.